Improved Sensorless Control of Interior Permanent Magnet Sensorless Motors Using an Active Damping Control Strategy

Authors:

Younghoon Cho

Date Submitted: 2018-11-27

Keywords: parameter variation, position estimator, extended electromotive force, sensorless drive, interior permanent magnet motor, active damping

Abstract:

This paper proposes the active damping control strategy for position sensorless operation of an interior permanent magnet (IPM) motor. The proposed method is applied to both the current controller and the position estimator to control damping characteristics of the IPM drive system. By actively increasing the damping characteristics of the system with the proposed method, the current control and the position estimation loops become immune to parameter variation of the stator resistance which may degrade the accuracy of the position estimator. To analyze the accuracy of the position estimator with and without the proposed method, a small-signal analysis is carried out for low speed operation where the effect of the parameter variation is relatively large due to a low signal-to-noise ratio (SNR). Additionally, an open-loop voltage to angular velocity transfer function including the electrical and the mechanical parameters is investigated. Since no hardware modifications are necessary, the proposed method can be easily implemented just in software routines. Both the simulations and the experimental validations in which the proposed active damping control strategy is incorporated with the existing extended electromotive force (EMF)- based sensorless algorithm are provided to support the effectiveness of the proposed method.

Record Type: Published Article

Submitted To: LAPSE (Living Archive for Process Systems Engineering)

Citation (overall record, always the latest version): LAPSE:2018.0869
Citation (this specific file, latest version): LAPSE:2018.0869-1
Citation (this specific file, this version): LAPSE:2018.0869-1v1

DOI of Published Version: https://doi.org/10.3390/en9030135

energies

MDPI

Article

Improved Sensorless Control of Interior Permanent Magnet Sensorless Motors Using an Active Damping Control Strategy

Younghoon Cho

Department of Electrical Engineering, Konkuk University, Seoul 05029, Korea;
yhcho98@konkuk.ac.kr; Tel.: +82-10-6207-0431; Fax: +82-447-9186

Academic Editor: K. T. Chau
Received: 11 January 2016; Accepted: 4 February 2016; Published: 26 February 2016

Abstract: This paper proposes the active damping control strategy for position sensorless operation of an interior permanent magnet (IPM) motor. The proposed method is applied to both the current controller and the position estimator to control damping characteristics of the IPM drive system. By actively increasing the damping characteristics of the system with the proposed method, the current control and the position estimation loops become immune to parameter variation of the stator resistance which may degrade the accuracy of the position estimator. To analyze the accuracy of the position estimator with and without the proposed method, a small-signal analysis is carried out for low speed operation where the effect of the parameter variation is relatively large due to a low signal-to-noise ratio (SNR). Additionally, an open-loop voltage to angular velocity transfer function including the electrical and the mechanical parameters is investigated. Since no hardware modifications are necessary, the proposed method can be easily implemented just in software routines. Both the simulations and the experimental validations in which the proposed active damping control strategy is incorporated with the existing extended electromotive force (EMF)- based sensorless algorithm are provided to support the effectiveness of the proposed method.

Keywords: active damping; interior permanent magnet motor; sensorless drive; extended electromotive force; position estimator; parameter variation

1. Introduction

Position sensors are necessary for high performance vector control of AC motors. However, popular position sensors such as optical encoders and resolvers are usually bulky, mechanically vulnerable, and may increase the implementation cost of the entire motor drive system. If the accuracy of the position sensor is unreliable, it may cause severe instability problems in the control loop. To overcome these drawbacks of position sensors, numerous control techniques where no position sensors are employed have been proposed [1]. The main purpose of sensorless control algorithms is to estimate the position and the speed of the motor without using a position or a speed sensor. In general, the realization of sensorless control can be classified into two categories: signal injection [2–7] and model-based methods [8–12]. In the signal injection methods, a high frequency voltage or current signal is directly utilized to estimate electrical position of the rotor by detecting inductance variation depending on rotor position and inductor saturation. These methods are generally suitable for low speed or zero speed operation due to additional losses and acoustic noise induced by injecting the voltage or current signal. The computational burden of implementing signal injection and filtering algorithms is an extra drawback.

The model-based methods mostly use electrical or electro-mechanical models of AC motors to estimate control parameters. Mostly, they extract the estimated states from back electromotive force (EMF) information. It means these methods cannot be directly applied under low speed or zero speed operation where back EMF information is rarely obtained. Many modern control schemes using a model reference adaptive system (MRAS), an adaptive observer, nonlinear control, and so on are proposed for sensorless AC motor drives [8–12]. In some cases, hybrid methods incorporating signal injection and model based methods are utilized to cover full operation range of the AC motor [13–17]. In many applications such as fans, compressors and blowers that normally have medium or high speed regions, the model-based methods are attractive [18–20].

Among many model-based sensorless methods, so-called extended EMF (EEMF)-based methods have been popularly adapted for IPM and synchronous reluctance motors where magnetic saliency exists [21–24]. However, the problem with these methods is that sensorless operation can fail due to parameter mismatches or variations, especially in low speed operation or mode transition [25]. In [26], online stator flux and resistance estimators are proposed to improve sensorless operation at low speed. A flux estimation algorithm that uses the phase current derivative without signal injection in low speed is presented in [27]. In [28], an online parameter estimation technique is employed to minimize the effects of parameter variations. In [29], the current measurement error and the inverter irregularities are analyzed, then a stator resistance estimator is proposed. The parameter identification and inverter error compensation algorithms based on the extended EMF method are presented in [30]. In [31,32], non-ideal characteristics of inverters such as output voltage phase delay and on-state resistance of the power devices are compensated to achieve performance improvement of the sensorless drive. However, the drawbacks of the aforementioned methods are that they are somewhat complicated to implement, and moreover, the performance of sensorless control is highly dependent on the accuracy of the position estimators and the compensation methods.

In this paper, an active damping control strategy is applied to improve the sensorless operation of the IPM motor. It is analyzed that low damping component in the entire control loop causes the failure of the sensorless operation under low speed or the mode transition between the open-loop acceleration and the sensorless mode. The proposed method artificially increases the damping component of the drive system so that the effects of parameter variations on the stator resistance are reduced. Therefore, stable sensorless operation in the low speed region where the signal-to-noise (SNR) is extremely low can be achieved, even with parameter mismatches between the physical system and the plant model. The small-signal analysis is taken to show the accuracy of the position estimator considering a practical parameter mismatch with and without the proposed method. From this, it is theoretically verified that the proposed method actively changes the damping component, and reduces the position estimation error. The open-loop voltage to angular velocity model is also derived to show the performance of the active damping control algorithm. Both the simulation and the experimental results for the IPM drive system show good agreement with the analyses, and the effectiveness of the proposed method are verified.

2. Extended EMF Based Sensorless Control of IPM Motor

In an IPM motor, the extended EMF E_{ex} is defined as [21,22]:

$$E_{ex} = \omega_r \left[\left(L_d - L_q \right) i_d + \lambda_f \right] - \left(L_d - L_q \right) \left(s i_q \right) \tag{1}$$

where s, ω_r, L_d, L_q, λ_f, i_d and i_q are the Laplace variable, the electrical angular velocity, the d-axis inductance, the q-axis inductance, the magnet flux linkage, and the d- and q-axes currents, respectively. By using Equation (1), the electrical model of IPM motors in the synchronous rotating frame is written as follows:

$$\begin{bmatrix} v_d \\ v_q \end{bmatrix} = \begin{bmatrix} R_s + sL_d & -\omega_r L_q \\ \omega_r L_q & R_s + sL_d \end{bmatrix} \begin{bmatrix} i_d \\ i_q \end{bmatrix} + \begin{bmatrix} 0 \\ E_{ex} \end{bmatrix} \tag{2}$$

where R_s, v_d, and v_q represents the stator resistance, the d-, and the q-axes voltages. It should be noted that L_q appears in both of d- and q-axes cross-coupling terms, and L_d is used in non-cross-coupling terms unlike the typical electrical model of IPM motors. Let us define γ-δ coordinate as the estimated axes obtained by using a proper sensorless algorithm. Then, the electrical model of IPM motors oriented to γ-δ coordinate is written as:

$$\begin{bmatrix} v_\gamma \\ v_\delta \end{bmatrix} = \begin{bmatrix} R_s + sL_d & -\omega_r L_q \\ \omega_r L_q & R_s + sL_d \end{bmatrix} \begin{bmatrix} i_\gamma \\ i_\delta \end{bmatrix} + \begin{bmatrix} e_\gamma \\ e_\delta \end{bmatrix} \tag{3}$$

where i_γ and i_δ represent the estimated γ- and δ-axis currents in γ-δ coordinate, and e_γ and e_δ are the estimated EMF components in γ-δ coordinate. Here, e_γ and e_δ are defined as [22]:

$$\begin{bmatrix} e_\gamma \\ e_\delta \end{bmatrix} = E_{ex} \begin{bmatrix} -\sin\left(\theta_r - \hat{\theta}_r\right) \\ \cos\left(\theta_r - \hat{\theta}_r\right) \end{bmatrix} + \left(\hat{\omega}_r - \omega_r\right) L_d \begin{bmatrix} -i_\delta \\ i_\gamma \end{bmatrix} \tag{4}$$

where θ_r, $\hat{\theta}_r$, and $\hat{\omega}_r$ are the actual electrical position, the estimated electrical position, and the estimated electrical angular velocity of the rotor.

Figure 1 shows the relationship between d-q and γ-δ coordinates. In sensorless operation, the second term in right-hand-side (RHS) in Equation (4) can be neglected by assuming L_d and the error between $\hat{\omega}_r$ and ω_r are small enough to be ignored after they are multiplied. By doing so, Equation (4) is simplified as Equation (5).

$$\begin{bmatrix} e_\gamma \\ e_\delta \end{bmatrix} \approx E_{ex} \begin{bmatrix} -\sin\left(\theta_r - \hat{\theta}_r\right) \\ \cos\left(\theta_r - \hat{\theta}_r\right) \end{bmatrix} \tag{5}$$

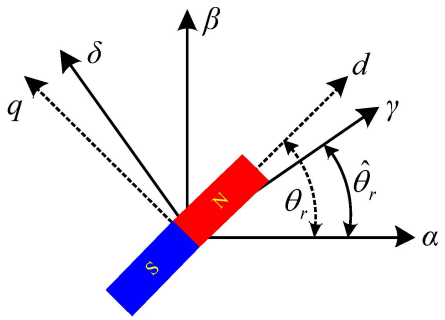

Figure 1. Relationship between d-q and γ-δ reference frames.

From Equation (5), the angle error θ_e between d-q and γ-δ coordinates is obtained as below:

$$\theta_e = \theta_r - \hat{\theta}_r = \tan^{-1}\left(-\frac{e_\gamma}{e_\delta}\right) \tag{6}$$

To calculate θ_e from Equation (6), Equation (3) is rearranged as follows:

$$\begin{aligned} e_\gamma &= v_\gamma + \omega_r L_q i_\delta - \left(R_s + sL_d\right) i_\gamma \\ e_\delta &= v_\delta - \omega_r L_q i_\gamma - \left(R_s + sL_d\right) i_\delta \end{aligned} \tag{7}$$

where v_γ and v_δ represent γ- and δ-axes voltages while i_γ and i_δ represent γ- and δ-axes currents. By substituting Equation (7) into Equation (6), θ_e can be calculated. In practice, a low pass filter is multiplied on the equations in (7) as:

$$\begin{bmatrix} e_{\gamma LPF} \\ e_{\delta LPF} \end{bmatrix} = \frac{\omega_{ci}}{s + \omega_{ci}} \begin{bmatrix} e_\gamma \\ e_\delta \end{bmatrix} \tag{8}$$

where ω_{ci} is the radian expression of the cutoff frequency f_{ci} for the first order low pass filter. The low pass filter which was reported as a part of the observer in [22] helps to avoid direct implementation of the differential terms which may be vulnerable for noise components in feedback paths. Then, $e_{\gamma LPF}$ and $e_{\delta LPF}$ are rewritten as follows:

$$\begin{aligned} e_{\gamma LPF} &= \frac{\omega_{ci}}{s+\omega_{ci}}\left(v_\gamma + \omega_r L_q i_\delta - R_s i_\gamma\right) - \frac{\omega_{ci} s}{s+\omega_{ci}} L_d i_\gamma \\ e_{\delta LPF} &= \frac{\omega_{ci}}{s+\omega_{ci}}\left(v_\delta - \omega_r L_q i_\gamma - R_s i_\delta\right) - \frac{\omega_{ci} s}{s+\omega_{ci}} L_d i_\delta \end{aligned} \tag{9}$$

In fact, by introducing the low pass filter, the first term $\omega_{ci}/(s+\omega_{ci})$ in RHS of Equation (9) is analyzed as the first order Pseudo integrator with the cut-off angular frequency ω_{ci} while the second term $s\omega_{ci}/(s+\omega_{ci})$ operates as the first order Pseudo differentiator which may be the same form with a high pass filter. Compared to Equation (7), Equation (9) gives much more stable operation in steady state with slightly less, but acceptable, dynamic performance in back EMF estimation.

Figure 2 shows the structures of the position and speed estimator. The fundamental idea shown in Figure 2a is to estimate $\hat{\theta}_r$ by tracking θ_e to be zero. In practice, θ_e is directly obtained from Equation 6 as can be seen in Figure 2b, because ω_r or θ_r is not directly available. The estimator $G_{est}(s)$ in Figure 2 can be implemented with a simple proportional-integrator (PI) compensator. The detailed design procedure of $G_{est}(s)$ is explained in [22]. The electrical angle estimation algorithm is widely used in many applications due to its simple implementation and good estimation performance. However, there are mainly two problems with the algorithm. One is that the estimation performance is not very good with inaccurate system parameters. Another is that low speed operation may be hard or even impossible due to the difficulty of obtaining the extended EMF components in such a low signal-to-noise ratio (SNR) condition.

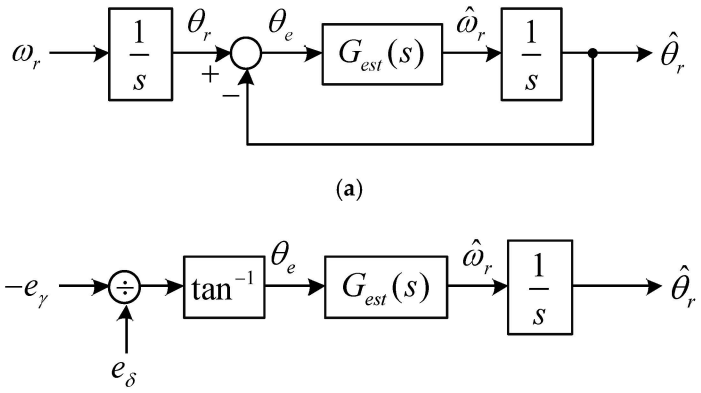

Figure 2. Structures of the position and speed estimator. (**a**) Basic concept. (**b**) Practical implementation.

3. Sensorless Control with Active Damping Control Strategy

The active damping technique used in this paper has been studied in several references [33–36] where the same concept may be called by different names. The basic concept of the active damping control is to artificially adjust the electrical damping of the motor drive system within the possible physical range by adding current feedback paths with a proper proportional gain. If the proportional gain is well selected, the stability and the dynamic performance of the control system can be improved [33–36]. In this paper, the active damping technique is combined with the back EMF estimation which is a part of the sensorless algorithm to achieve stable operation and superior dynamics of the IPM motor drive system.

3.1. Back EMF Estimation with Active Damping Control

The proposed back EMF estimation scheme using the active damping resistance R_{dp} is shown in Figure 3 where $v_{\gamma\_ff} = \hat{\omega}_r L_q i_\delta$ and $v_{\delta\_ff} = -\hat{\omega}_r L_q i_\gamma$. Here, R_{dp} is added only to the estimated current feedback paths.

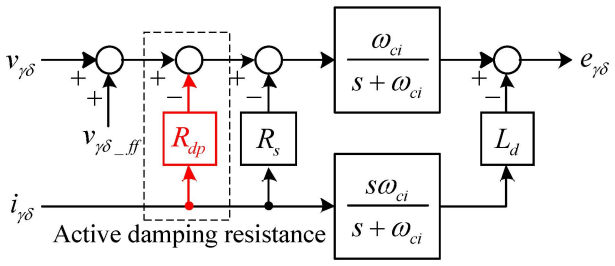

Figure 3. Back EMF estimation method using the active damping resistance.

The estimated back EMF components after passing the low pass filter can be written as follows.

$$\begin{aligned} e_{\gamma LPF} &= \frac{\omega_{ci}}{s+\omega_{ci}}\left(v_\gamma + v_{\gamma\_ff} - \left(R_s + R_{dp}\right) i_\gamma\right) - \frac{\omega_{ci} s}{s+\omega_{ci}} L_d i_\gamma \\ e_{\delta LPF} &= \frac{\omega_{ci}}{s+\omega_{ci}}\left(v_\delta + v_{\delta\_ff} - \left(R_s + R_{dp}\right) i_\delta\right) - \frac{\omega_{ci} s}{s+\omega_{ci}} L_d i_\delta \end{aligned} \tag{10}$$

Note that Equation (10) has the same form as Equation (9) except R_{dp} is added to R_s. The equations in (10) imply that the tendency of the back EMF and angle estimation characteristics can be adjusted by R_{dp}. In order to see how R_{dp} affects the estimation performance, the small signal analysis for θ_e will be discussed hereafter. For convenience of the analysis, the first order Pseudo integrator and differentiator are neglected. Then, i_δ can be rearranged as in Equation (11):

$$i_\delta = \frac{v_\delta - \omega_r L_q i_\gamma - e_\delta}{L_d s + (R_s + R_{dp})} \tag{11}$$

By substituting Equation (11) into e_γ, we have:

$$e_\gamma = v_\gamma + \omega_r L_q \left(\frac{v_\delta - \omega_r L_q i_\gamma - e_\delta}{L_d s + (R_s + R_{dp})}\right) - \left((R_s + R_{dp}) + s L_d\right) i_\gamma \tag{12}$$

If the operational speed and the inertia of the IPM motor are low and high enough, it is possible to assume that the differentiation of the mechanical speed is zero. After that, e_γ can be simplified as in Equation (13) by considering the perturbation:

$$\tilde{e}_\gamma = -\frac{\omega_r L_q \tilde{e}_\delta}{L_d s + (R_s + R_{dp})} \tag{13}$$

Equation (13) can be rearranged as below:

$$-\frac{\tilde{e}_\gamma}{\tilde{e}_\delta} = \frac{\omega_r L_q}{L_d s + (R_s + R_{dp})} \tag{14}$$

By substituting Equation (14) into Equation (6), the small signal model of the electrical angle error $\tilde{\theta}_e$ is obtained as follows:

$$\tilde{\theta}_e = \tan^{-1}\left(-\frac{\tilde{e}_\gamma}{\tilde{e}_\delta}\right) = \tan^{-1}\left(\frac{\omega_r L_q}{L_d s + (R_s + R_{dp})}\right) \tag{15}$$

If $\tilde{\theta}_e$ changes within a very limited range, e.g., –0.2 rad < $\tilde{\theta}_e$ < 0.2 rad, (15) can be simplified even more as below:

$$\tilde{\theta}_e = \tan^{-1}\left(\frac{\omega_r L_q}{L_d s + (R_s + R_{dp})}\right) \approx \frac{\omega_r L_q}{L_d s + (R_s + R_{dp})} \tag{16}$$

Figure 4 compares the frequency responses of $\tilde{\theta}_e$ at different R_{dp} values where L_d = 2.51 mH, L_q = 6.94 mH, R_s = 0.09 Ω, and ω_r = 18.85 rad/s. As can be seen in the figure, the magnitude of $\tilde{\theta}_e$ is getting lower as R_{dp} increasing. If all parameters and variables are constant in (16) except R_{dp}, the gain of the transfer function is reduced as R_{dp} increases. This implies that even if the back EMF estimation is not very stable, the electrical angle error is smaller with larger R_{dp}. In other words, the angle estimation is better with R_{dp} in transients and some conditions where the back EMF estimation is oscillatory.

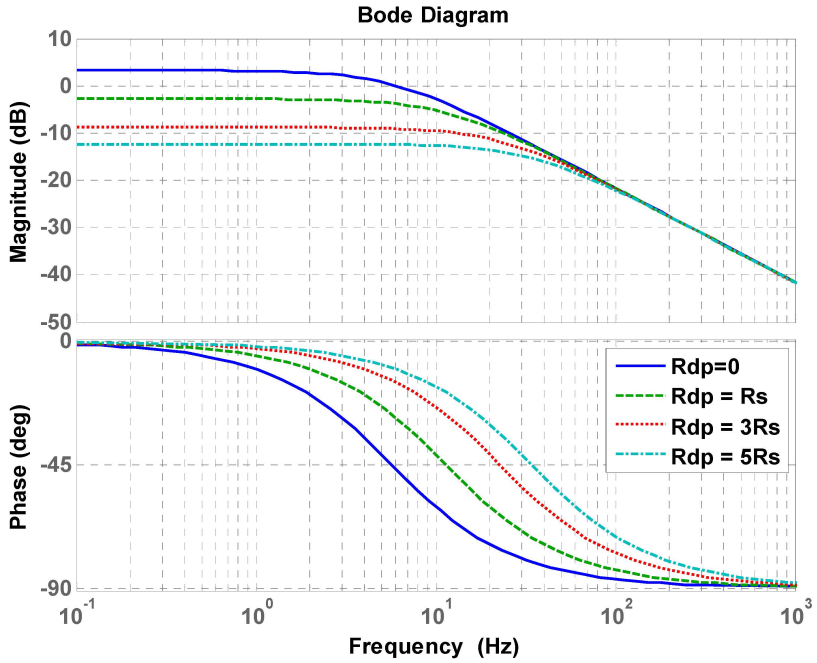

Figure 4. Comparison of the frequency responses of $\tilde{\theta}_e$ at different R_{dp}.

The trajectories of the position error variation depending on the ratio of the BEMF variation are plotted in Figure 5. As illustrated in the figure, the variation of the position error becomes smaller as R_{dp} is increased. This trend also matches the analysis taken previously.

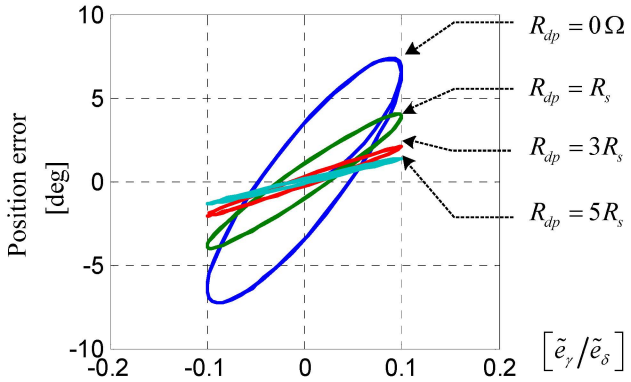

Figure 5. Trajectories of the position error variation.

3.2. Current Control Strategy with Active Damping Control

If R_{dp} is used for the back EMF estimation, it is better to use R_{dp} even in the current controller to reduce the model mismatch between the actual and the estimated control system as shown in Figure 6.

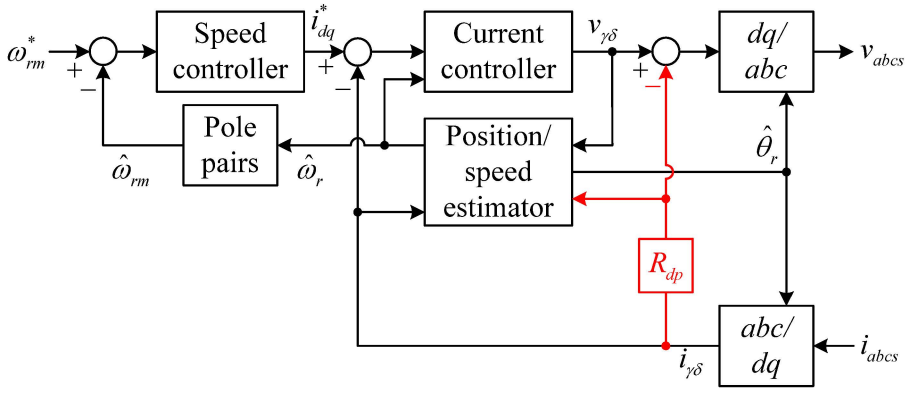

Figure 6. Sensorless control algorithm with the active damping control strategy.

Figure 7 shows the current controller implementation with R_{dp}. Note that the current controller consists of a PI controller as a feedback controller and a decoupling terms v_{dq_ff} as follows:

$$\begin{bmatrix} v_{d\_ff} \\ v_{q\_ff} \end{bmatrix} = \begin{bmatrix} 0 & -\omega_r \\ \omega_r & 0 \end{bmatrix} \begin{bmatrix} L_d & 0 \\ 0 & L_q \end{bmatrix} \begin{bmatrix} i_d \\ i_q \end{bmatrix} \tag{17}$$

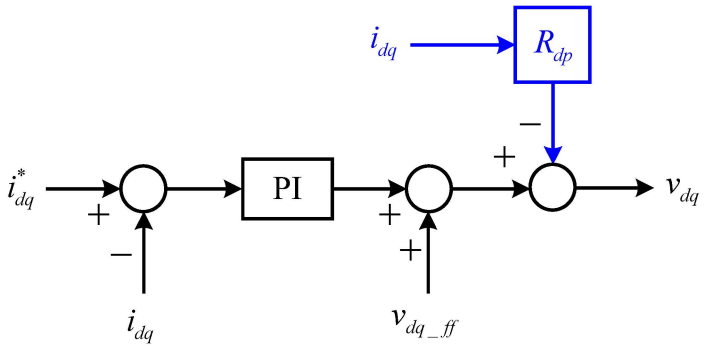

Figure 7. Current controller implementation with R_{dp}.

The gain of the PI controllers is selected as:

$$\begin{aligned} K_{pd} &= \omega_c L_d K_{pq} = \omega_c L_q \\ K_{id} &= K_{iq} = \omega_c \left(R_s + R_{dp} \right) \end{aligned} \tag{18}$$

where K_{pd}, K_{pq}, K_{id}, K_{iq}, and ω_c represent d-, q-axes proportional gains, d-, q-axes integral gain, and desired bandwidth of the current controller, respectively. Note that R_{dp} is included to the integral gain. By selecting the control gain this way and using the feed-forward terms, the overall characteristics of the entire control system can be emulated as a simple low pass filter whose cutoff frequency is the same to the bandwidth of the control system, as expressed in Equation (19).

$$\frac{i_{dq}(s)}{i^*_{dq}(s)} \simeq \frac{\omega_c}{s + \omega_c} \tag{19}$$

This is so-called the technical optimization of current controllers [37]. Equation (19) implies that the current control bandwidth is identical to ω_c, and the phase margin is 90°.

To examine the effect of R_{dp} in the current control loop, a simple voltage to mechanical speed model will be derived hereafter. Let us consider the torque equation of the IPM motor as below:

$$T_e = \frac{3}{2}\frac{P}{2}\left(\lambda_f i_q + \left(L_d - L_q\right) i_d i_q\right) \tag{20}$$

where P is the number of poles. In order to simplify the analysis, i_d is assumed to be zero, then we have:

$$T_e = \frac{3}{2}\frac{P}{2}\lambda_f i_q = K_T i_q\,, \quad \text{where } K_T \equiv \frac{3}{4}K_E \text{ and } K_E \equiv P\lambda_f \tag{21}$$

The block diagram of q-axis voltage-to-mechanical speed is shown in Figure 8, whose parameters are denoted in Table 1. In order to see the effect of R_{dp} only, the feedback controllers are excluded in this analysis. From Figure 8, the transfer function of v_q- to -ω_{rm} is given as Equation (22):

$$G_{v\omega}(s) = \frac{\omega_{rm}}{v_q} = \frac{K_T}{\left(sL_q + \left(R_s + R_{dp}\right)\right)\left(J_m s + B_m\right) + K_T K_E} \tag{22}$$

where J_m and B_m are the inertia moment and the friction coefficients of the mechanical system. Figure 9 compares the frequency response of Equation (22) with different R_{dp} values. The highest resonance occurs with no R_{dp}. The resonance means that ω_{rm} is oscillatory when v_q which is the output of the feedback controller changes quickly in cases such as a step load variation. If R_{dp} is increased, the resonance is getting damped. When R_{dp} is selected to be $10R_s$, the resonance is almost nothing so that the frequency response of the transfer function is similar to a first order low pass filter. In this case, ω_{rm} may not fluctuate that much even in the step load variation. Accordingly, it is supposed that the use of R_{dp} definitely helps to stabilize the speed control loop of the motor drive system.

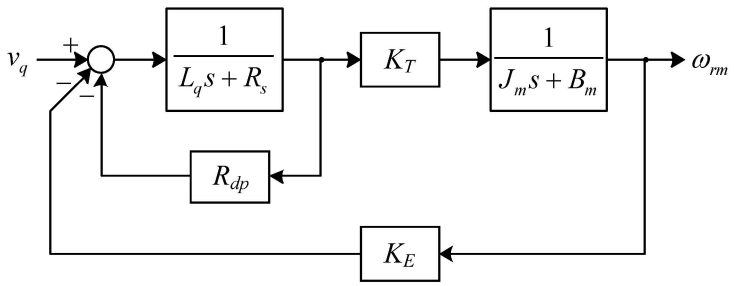

Figure 8. Block diagram to examine the effect of R_{dp}.

Table 1. Motor parameters.

Parameters	Values
Number of poles (P)	6
Magnet flux linkage (λ_f)	0.235 V/(rad/s)
d-axis inductance (L_d)	2.51 mH
q-axis inductance (L_q)	6.94 mH
Stator resistance (R_s)	0.09 Ω
Rotor inertia (J_m)	0.003334 kg·m^2
Friction constant (B_m)	0.425×10^{-3}·m^2/s
Rated speed	1600 rev/min
Rated torque	65 Nm

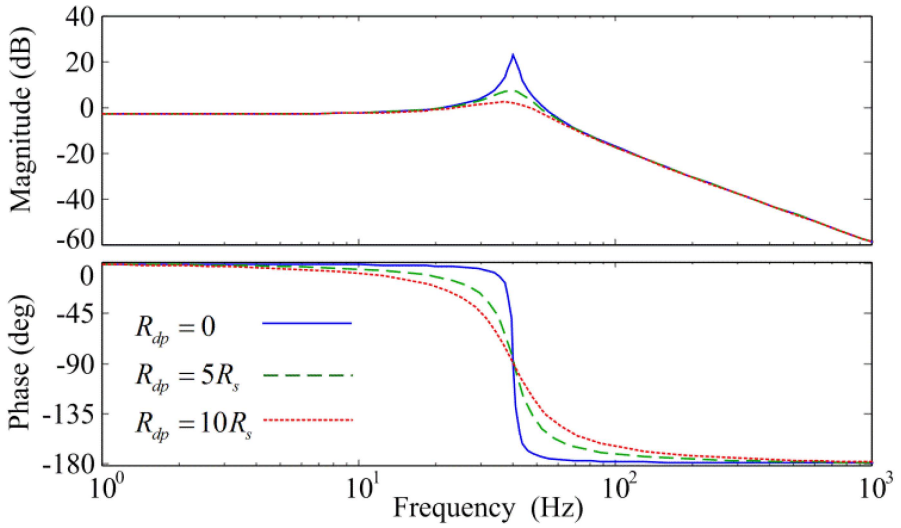

Figure 9. Frequency response of $G_{v\omega}$(s) under different R_{dp} conditions.

4. Simulation Study

Simulations have been carried out to examine the performance of the proposed method on the sensorless control. The parameters in the simulations are the same with Table 1. The speed reference profile and the operation mode for the simulations are shown in Figure 10. To start the IPM motor, the well-known open-loop synchronous acceleration method [19,20] is applied. The EEMF based sensorless algorithm is also utilized to estimate the position and the speed of the IPM motor. The mode transition from the open-loop synchronous acceleration to the sensorless control occurs at 60 RPM.

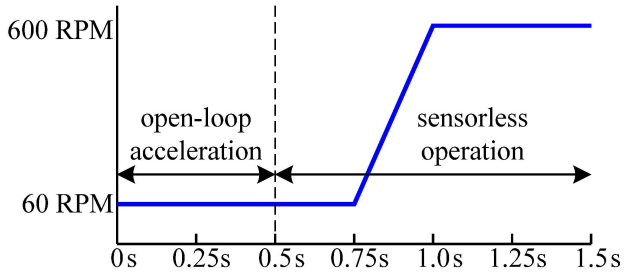

Figure 10. The profile of the speed reference and the operation modes.

Figure 11 shows the simulation results where the parameter mismatches in the current controller and the position and the speed estimator are intentionally inserted. At the start, 10% of the rated torque is applied. After 0.5 s, the operation mode is switched from the open-loop synchronous acceleration to the sensorless mode. After the speed of the motor is increased to 500 RPM, 30% of the rated torque is applied at t = 1.25 s. In each figure, the red dashed line, the green dotted line, and the blue solid line represent the cases when R_{dp} equals to zero, $3\hat{R}_s$, and $5\hat{R}_s$.

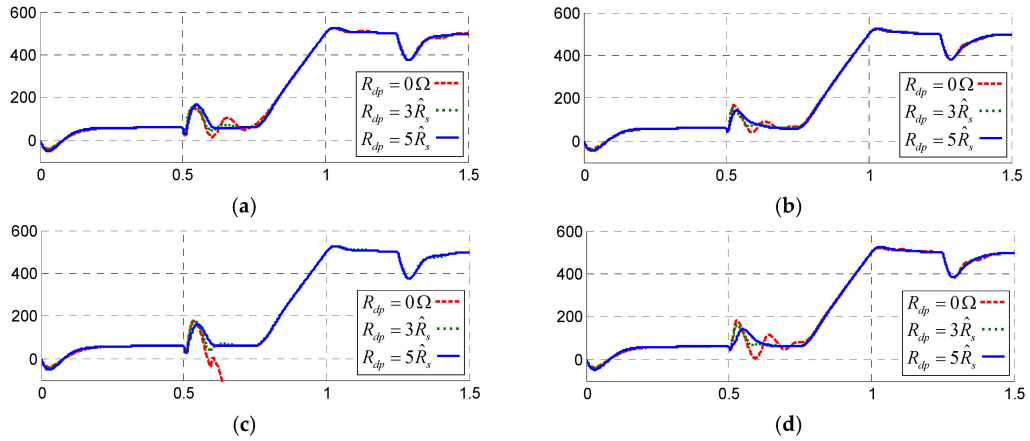

Figure 11. Simulation results. (**a**) $\hat{R}_s = 0.75R_s$, $\hat{L}_{dq} = 0.75L_{dq}$, and $\hat{\lambda}_f = 1.15\lambda_f$; (**b**) $\hat{R}_s = 0.75R_s$, $\hat{L}_{dq} = 1.25L_{dq}$, and $\hat{\lambda}_f = 1.15\lambda_f$; (**c**) $\hat{R}_s = 1.25R_s$, $\hat{L}_{dq} = 0.75L_{dq}$, and $\hat{\lambda}_f = 1.15\lambda_f$; (**d**) $\hat{R}_s = 1.25R_s$, $\hat{L}_{dq} = 1.25L_{dq}$, and $\hat{\lambda}_f = 1.15\lambda_f$.

In each case in Figure 11, the responses without R_{dp} show more fluctuation than the cases with R_{dp}, where the response is much more damped at the mode transition from the open-loop synchronous acceleration to the sensorless operation. This is especially apparent in Figure 11c where the system failed to switch the operation mode to the sensorless control. These results correspond to the analysis in the previous sections, and show that the mode transition is made more stable by using R_{dp}. This implies that R_{dp} helps the stabilization of the IPM motor drive system undergoing the mode transition in the low speed region. Once the motor speed is over 500 RPM, the responses of a 30% load step condition are similar in all of the cases. From this result, it can be inferred that the utilized R_{dp} does not affect the normal sensorless operation where the motor speed is high enough to overcome low SNR on the estimated EMF components. However, it should be noted that the feedback current multiplied by R_{dp} is not a real-time current, but a sampled current, which has a zero-order-hold (ZOH) effect. Hence, the feedback current may not be the same with an ideal case, because the high frequency components are delayed in the feedback. The limitation of the output voltage is also another issue. If the feedback current multiplied by R_{dp} is too high, the output voltage reference may be over the physical limitation of the output voltage. Therefore, too high value of R_{dp} may cause other instability issues in the system due to the ZOH effect and the output voltage limitation.

5. Experiments

Experiments have been performed to show the effectiveness of the proposed method. Figure 12 shows the experimental configuration.

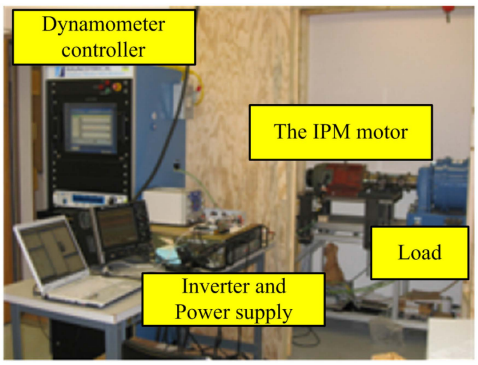

Figure 12. Experimental configuration.

The dc-link voltage is selected as 300V and it is fed by a dc power supply. The same motor parameters described in Table 1 are utilized for the experiments. The specifications of control parameters are shown in Table 2.

Table 2. Control parameters.

Parameters	Values
Switching frequency	10 kHz
Sampling frequency	10 kHz
Current control bandwidth	300 Hz
Position estimator bandwidth	100 Hz
Crossover frequency of the Pseudo integrator and differentiator	100 Hz

The proposed algorithm is implemented with a custom made digital control board in which a 32-bit digital signal processor is employed. The control board includes a 4-channel digital-to-analog converter (DAC) to monitor the internal variables in the software routines. A 13-bit external encoder is connected to the IPM motor to compare the real and the estimated position of the rotor. A Magtrol dynamometer is utilized to apply loads and to measure the motor torque. Although the testing motor is an IPM motor, the d-axis current reference is selected as zero to simplify confirming the validation of the proposed algorithm where a maximum torque per ampere is not necessary. However, the operational principle should not be different even in flux weakening region. In the experiments, the magnet flux linkage, the stator resistance, the d- and the q-axes inductances in the controller is selected as $0.9\lambda_f$, $0.75R_s$, $1.15L_d$, and $1.15L_q$ to artificially emulate the parameter mismatch condition. The active damping component R_{dp} is selected as $5\hat{R}_s$. In Figure 13, the sensorless operation with 10% of the rated torque is shown. Figure 13a shows the mode transition from the open-loop synchronous acceleration to the sensorless operation. The speed at the transition point is 120 RPM. As can be seen in the figure, the operation mode is smoothly switched. Figure 13b shows the steady state operation of the sensorless control, which is very stable. In both Figure 13a,b the oscilloscope channels 3 and channel 4 represent the actual electrical position θ_r measured by the 13-bit encoder and the estimated position $\hat{\theta}_r$. Channel 1 and channel 2 indicate the estimated EMFs e_γ and e_δ. The values of e_γ and e_δ are evaluated as 0 V and 8.86 V. These numbers agree with the results obtained from (3) when no errors occur. Hence, the position and the EMFs estimation are smooth, even with R_{dp}.

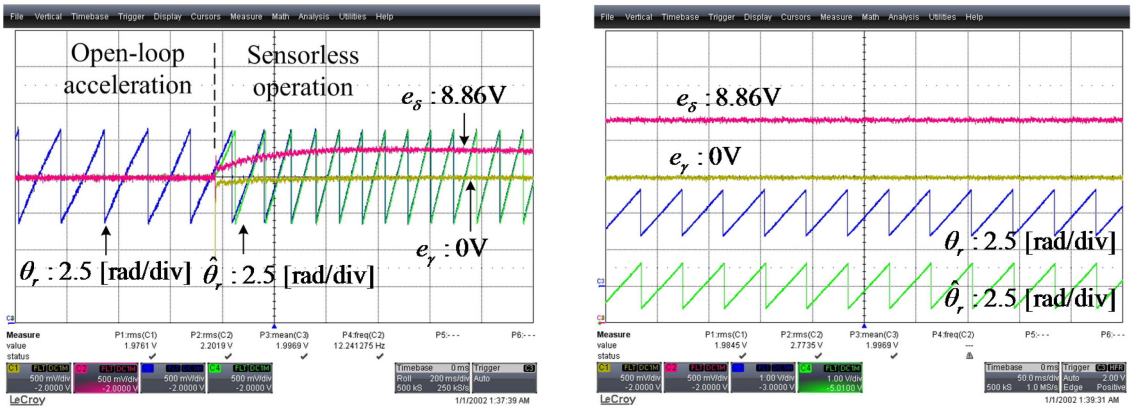

(**a**) (**b**)

Figure 13. Test results of the sensorless operation: (**a**) Mode transition; (**b**) Steady state.

Figure 14 shows the test results of a deceleration where the speed reference is changed from 500 RPM to 60 RPM in ramp. Here, 30% of the rated torque is applied as the load. In both cases, the estimated EMF value and the speed control performance are within the normal range at the beginning.

However, as seen in Figure 14a, the position and the EMF estimation fail and the speed is not regulated as the operating speed decreases without Rdp. This is due to the low SNR on the iterated values in the controller, the parameter mismatches, and the low system damping characteristic. Meanwhile, in Figure 14b, the stable sensorless operation is achieved with Rdp after slight transients at the beginning of 60 RPM operation under the same test condition.

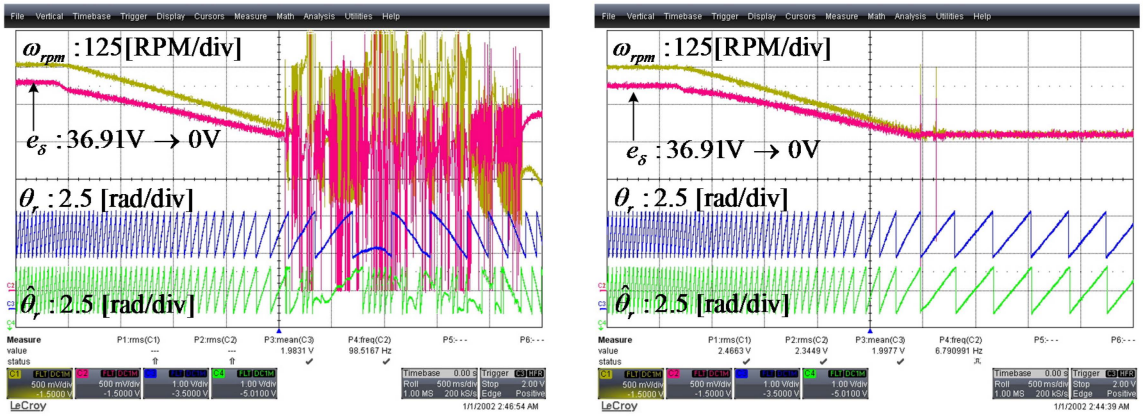

(**a**) (**b**)

Figure 14. Deceleration test results: (**a**) $R_{dp} = 0\Omega$ (**b**) $R_{dp} = 5\hat{R}_s$.

Figure 15 compares the trajectories of the position error θ_e which depends on the estimated EMF ratio e_γ/e_δ. The operating speed is 90 RPM and no load torque is applied. As analyzed in the previous section, the dispersion of the error trajectory with R_{dp} is narrower than the case without R_{dp}. It means the performance of the position estimation is accurate with the active damping resistance.

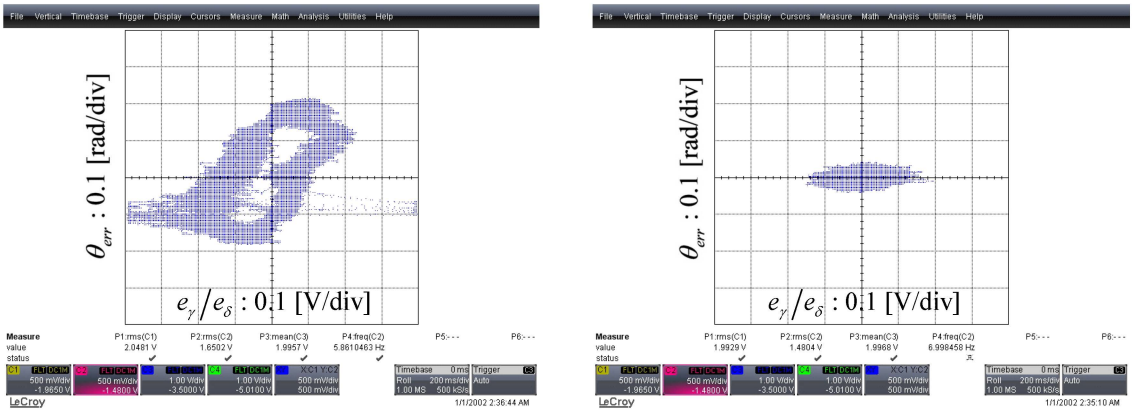

(**a**) (**b**)

Figure 15. Comparison of the trajectories of θ_e: (**a**) $R_{dp} = 0\Omega$ (**b**) $R_{dp} = 5\hat{R}_s$.

Figure 16 compares the position and the EMF estimation performance without and with R_{dp}. The same operating condition as in Figure 15 is assumed. As shown in the figure, the peak to peak fluctuation of the estimated EMF and the position are evaluated as about 20V and 0.35 rad before applying R_{dp}. However, the magnitudes are decreased to 3V and 0.18 rad with R_{dp}. The ripple components in the estimated EMF and the position are also reduced.

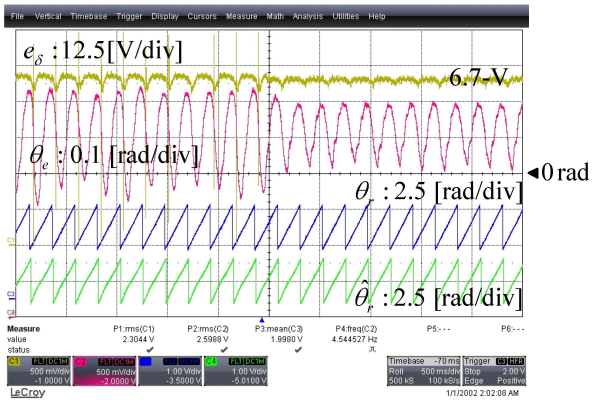

Figure 16. The position and the EMF estimation performance.

Figure 17 illustrates the test results on the torque and the speed response. The speed reference is 60 RPM and the applied load torque is 5% of the rated torque. In Figure 17a, the magnitude of the torque ripple is reduced from 3Nm to 1Nm after applying R_{dp}. The range of the speed fluctuation is also limited from 40 RPM to 10 RPM with R_{dp}.

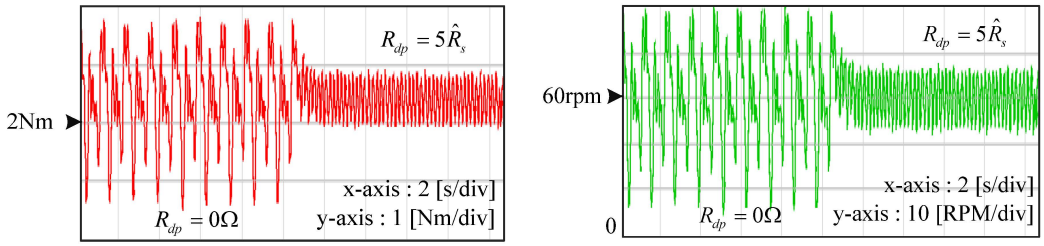

Figure 17. Torque and speed response without and with R_{dp}. (**a**) Torque response; (**b**) Speed response.

Figure 18 compares the step load test performance. 50% of the rated torque is applied using the Magtrol dynamometer. As can be seen in the comparison, if R_{dp} is not utilized, the speed regulation fails when the load is applied. With R_{dp}, although the minimum speed reaches 10 RPM, the speed regulation is recovered in steady state. In the experimental results, by using the proposed method, it is confirmed that the EMF and the position estimation performance and the stability of the system are improved even with the parameter mismatches.

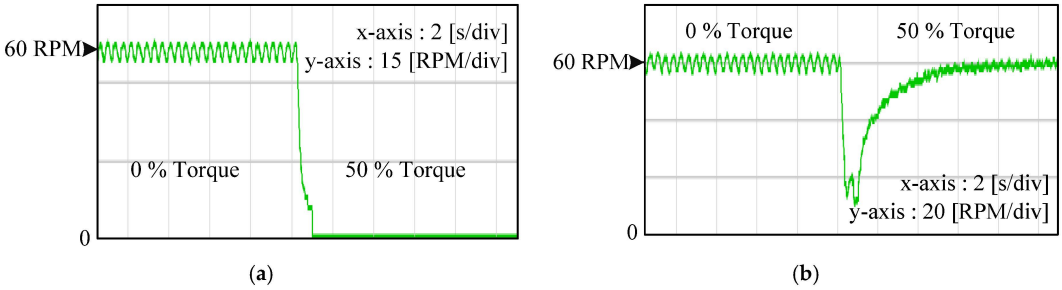

Figure 18. Speed response (**a**) without R_{dp} (**b**) with R_{dp}.

6. Conclusions

This paper proposed an active damping control strategy for the sensorless control of an IPM motor. The proposed method reduces the effects of the parameter mismatches, and increases the

damping characteristics of the overall control system. Accordingly, the stability of the control system is improved. The small signal analysis for the position error and the frequency response of the open-loop voltage-to-speed transfer function are performed to evaluate the stability of the system using the proposed method. The proposed algorithm is adapted to the EEMF based sensorless method. Both the simulations and the experiments agree that the EMF and the position estimation performance are improved, and the torque and the speed ripple are reduced.

Acknowledgments: All sources of funding of the study should be disclosed. Please clearly indicate grants that you have received in support of your research work. Clearly state if you received funds for covering the costs to publish in open access.

Conflicts of Interest: The author declares no conflict of interest.

References

1. Acarnley, P.P.; Watson, J.F. Review of position-sensorless operation of brushless permanent-magnet machines. *IEEE Trans. Ind. Electron.* **2006**, *53*, 352–362. [CrossRef]
2. Ha, J.I.; Ide, K.; Sawa, T.; Sul, S.K. Sensorless rotor position estimation of an interior permanent-magnet motor from initial states. *IEEE Trans. Ind. Appl.* **2003**, *39*, 761–767.
3. Shi, J.L.; Liu, T.H.; Chang, Y.C. Position control of an interior permanent-magnet synchronous motor without using a shaft position sensor. *IEEE Trans. Ind. Electron.* **2007**, *54*, 1989–2000.
4. Kasa, N.; Watanabe, H. A mechanical sensorless control system for salient-pole brushless DC motor with autocalibration of estimated position angles. *IEEE Trans. Ind. Electron.* **2000**, *47*, 389–395. [CrossRef]
5. Raca, D.; Garcia, P.; Reigosa, D.D.; Briz, F.; Lorenz, R.D. Carrier-signal selection for sensorless control of PM synchronous machines at zero and very low speeds. *IEEE Trans. Ind. Appl.* **2010**, *46*, 167–178. [CrossRef]
6. Reigosa, D.D.; Garcia, P.; Raca, D.; Briz, F.; Lorenz, R.D. Measurement and adaptive decoupling of cross-saturation effects and secondary saliencies in sensorless controlled IPM synchronous machines. *IEEE Trans. Ind. Appl.* **2008**, *44*, 1758–1767. [CrossRef]
7. Yoon, Y.D.; Sul, S.K.; Morimoto, S.; Ide, K. High bandwidth sensorless algorithm for AC machines based on square-wave type voltage injection. In Proceedings of the 2009 IEEE Energy Conversion Congress and Exposition, San Jose, CA, USA, 20–24 September 2009; pp. 2123–2130.
8. Hajian, M.; Soltani, J.; Markadeh, G.A.; Hosseinnia, S. Adaptive nonlinear direct torque control of sensorless IM drives with efficiency optimization. *IEEE Trans. Ind. Electron.* **2010**, *57*, 975–985. [CrossRef]
9. Kim, M.; Sul, S.K. An enhanced sensorless control method for PMSM in rapid accelerating operation. In Proceedings of the 2010 International Power Electronics Conference (IPEC), Sapporo, Japan, 21–24 June 2010; pp. 2249–2253.
10. Matsui, N. Sensorless PM brushless DC motor drives. *IEEE Trans. Ind. Electron.* **1996**, *43*, 300–308. [CrossRef]
11. Orlowska-Kowalska, T.; Dybkowski, M. Stator-current-based MRAS estimator for a wide range speed-sensorless induction-motor drive. *IEEE Trans. Ind. Electron.* **2010**, *57*, 1296–1308. [CrossRef]
12. Piippo, A.; Hinkkanen, M.; Luomi, J. Analysis of an adaptive observer for sensorless control of interior permanent magnet synchronous motors. *IEEE Trans. Ind. Electron.* **2008**, *55*, 570–576. [CrossRef]
13. Foo, G.; Rahman, M.F. Sensorless sliding-mode MTPA control of an IPM synchronous motor drive using a sliding-mode observer and HF signal injection. *IEEE Trans. Ind. Electron.* **2010**, *57*, 1270–1278. [CrossRef]
14. Mizutani, R.; Takeshita, T.; Matsui, N. Current model-based sensorless drives of salient-pole PMSM at low speed and standstill. *IEEE Trans. Ind. Appl.* **1998**, *34*, 841–846. [CrossRef]
15. Sayeef, S.; Foo, G.; Rahman, M.F. Rotor position and speed estimation of a variable structure direct-torque-controlled IPM synchronous motor drive at very low speeds including standstill. *IEEE Trans. Ind. Electron.* **2010**, *57*, 3715–3723. [CrossRef]
16. Foo, G.; Sayeef, G.; Rahman, M.F. Low-speed and standstill operation of a sensorless direct torque and flux controlled IPM synchronous motor drive. *IEEE Trans. Energy Convers.* **2010**, *25*, 25–33. [CrossRef]
17. Boldea, I.; Paicu, M.C.; Andreescu, G.D.; Blaabjerg, F. Active flux DTFC-SVM sensorless control of IPMSM. *IEEE Trans. Energy Convers.* **2009**, *24*, 314–322. [CrossRef]
18. Raggl, K.; Warberger, B.; Nussbaumer, T.; Burger, S.; Kolar, J.W. Robust angle-sensorless control of a PMSM bearingless pump. *IEEE Trans. Ind. Electron.* **2009**, *56*, 2076–2085. [CrossRef]

19. Rho, M.S.; Kim, S.M. Development of robust starting system using sensorless vector drive for a microturbine. *IEEE Trans. Ind. Electron.* **2010**, *57*, 1063–1073.
20. Yim, J.S.; Lee, W.J.; Sul, S.K.; Yang, H.S.; Kim, J.T. Sensorless vector control of super high speed turbo compressor. In Proceedings of the Twentieth Annual IEEE Applied Power Electronics Conference and Exposition, Austin, TX, USA, 6–10 March 2005; pp. 950–953.
21. Zhiqian, C.; Tomita, M.; Doki, S.; Okuma, S. An extended electromotive force model for sensorless control of interior permanent-magnet synchronous motors. *IEEE Trans. Ind. Electron.* **2003**, *50*, 288–295. [CrossRef]
22. Morimoto, S.; Kawamoto, K.; Sanada, M.; Takeda, Y. Sensorless control strategy for salient-pole PMSM based on extended EMF in rotating reference frame. *IEEE Trans. Ind. Appl.* **2002**, *38*, 1054–1061. [CrossRef]
23. Ichikawa, S.; Tomita, M.; Doki, S.; Okuma, S. Sensorless control of synchronous reluctance motors based on extended EMF models considering magnetic saturation with online parameter identification. *IEEE Trans. Ind. Appl.* **2006**, *42*, 1264–1274. [CrossRef]
24. Hasegawa, M.; Yoshioka, S.; Matsui, K. Position sensorless control of interior permanent magnet synchronous motors using unknown input observer for high-speed drives. *IEEE Trans. Ind. Appl.* **2009**, *45*, 938–946. [CrossRef]
25. Ribeiro, L.A.d.S.; Harke, M.C.; Lorenz, R.D. Dynamic properties of back-EMF based sensorless drives. In Proceedings of the 41st IAS Annual Meeting on Industry Applications Conference, Tampa, FL, USA, 8–12 October 2006; pp. 2026–2033.
26. Foo, G.; Rahman, M.F. Sensorless direct torque and flux-controlled IPM synchronous motor drive at very low speed without signal injection. *IEEE Trans. Ind. Electron.* **2010**, *57*, 395–403. [CrossRef]
27. Vogelsberger, M.A.; Grubic, S.; Habetler, T.G.; Wolbank, T.M. Using PWM-induced transient excitation and advanced signal processing for zero-speed sensorless control of ac machines. *IEEE Trans. Ind. Electron.* **2010**, *57*, 365–374. [CrossRef]
28. Morimoto, S.; Sanada, M.; Takeda, Y. Mechanical sensorless drives of IPMSM with online parameter identification. *IEEE Trans. Ind. Appl.* **2006**, *42*, 1241–1248. [CrossRef]
29. Mobarakeh, B.N.; Tabar, F.M.; Sargos, F.M. Back EMF estimation-based sensorless control of PMSM: Robustness with respect to measurement errors and inverter irregularities. *IEEE Trans. Ind. Appl.* **2007**, *43*, 485–494. [CrossRef]
30. Inoue, Y.; Yamada, K.; Morimoto, S.; Sanada, M. Effectiveness of voltage error compensation and parameter identification for model-based sensorless control of PMSM. *IEEE Trans. Ind. Appl.* **2009**, *45*, 213–221. [CrossRef]
31. Genduso, F.; Miceli, R.; Rando, C.; Galluzzo, G.R. Back EMF sensorless-control algorithm for high-dynamic performance PMSM. *IEEE Trans. Ind. Electron.* **2010**, *57*, 2092–2100. [CrossRef]
32. Raute, R.; Caruana, C.; Staines, C.S.; Cilia, J.; Sumner, M.; Asher, G.M. Analysis and compensation of inverter nonlinearity effect on a sensorless PMSM drive at very low and zero speed operation. *IEEE Trans. Ind. Electron.* **2010**, *57*, 4065–4074. [CrossRef]
33. Kim, H.; Lorenz, R.D. Synchronous frame PI current regulators in a virtually translated system. In Proceedings of the 39th IAS Annual Meeting on Industry Applications Conference, Seattle, WA, USA, 3–7 October 2004; pp. 856–863.
34. Kim, H.; Lorenz, R.D. A virtual translation technique to improve current regulator for salient-pole AC machines. In Proceedings of the 2004 IEEE 35th Annual Power Electronics Specialists Conference, Aachen, Germany, 20–25 June 2004; pp. 487–493.
35. Yang, S.M.; Su, P.D. Active damping control of hybrid stepping motor. In Proceedings of the 2001 4th IEEE International Conference on Power Electronics and Drive Systems, Denpasar, Indonesia, 22–25 October 2001; pp. 749–754.
36. Yim, J.S.; Sul, S.K.; Bae, B.H.; Patel, N.R.; Hiti, S. Modified current control schemes for high-performance permanent-magnet AC drives with low sampling to operating frequency ratio. *IEEE Trans. Ind. Appl.* **2009**, *45*, 763–771. [CrossRef]
37. Sul, S.K. *Control of Electric Machine Drive System*, 1st ed.; Brain Korea: Seoul, Korea, 2002.